The Astrophysical Journal Letters, 992:L29 (9pp), 2025 October 20 https://doi.org/10.3847/2041-8213/ae0c08

Extreme Negative Polarization of New Interstellar Comet 3I/ATLAS

Zuri Gray[1], Stefano Bagnulo[2], Galin Borisov[3,2], Yuna G. Kwon[4], Alberto Cellino[5], Ludmilla Kolokolova[6], Rosemary C. Dorsey[1], Grigori Fedorets[1,7], Mikael Granvik[1,8], Eric MacLennan[1], Olga Muñoz[9], Philippe Bendjoya[10], Maxime Devogèle[11], Simone Ieva[12], Antti Penttilä[1], and Karri Muinonen[1]
[1] Department of Physics, University of Helsinki, P.O. Box 64, 00014, Finland
[2] Armagh Observatory & Planetarium, College Hill, Armagh BT61 9DG, UK
[3] Institute of Astronomy and National Astronomical Observatory, Bulgarian Academy of Sciences, 72 Tsarigradsko Chaussée Blvd, BG-1784 Sofia, Bulgaria
[4] Caltech/IPAC, 1200 E California Blvd, MC 100-22, Pasadena, CA 91125, USA
[5] INAF—Osservatorio Astrofisico di Torino, I-10025 Pino Torinese, Italy
[6] Department of Astronomy, University of Maryland, College Park, MD 20742-2421, USA
[7] Finnish Centre for Astronomy with ESO, University of Turku, FI-20014 Turku, Finland
[8] Asteroid Engineering Laboratory, Luleå University of Technology, Box 848, SE-98128 Kiruna, Sweden
[9] Instituto de Astrofísica de Andalucía, CSIC, Glorieta de la Astronomia s/n, E-18008 Granada, Spain
[10] Université Côte d'Azur, Laboratoire Lagrange, OCA, CNRS UMR 7293, Nice, France
[11] ESA NEO Coordination Centre, Largo Galileo Galilei 1, I-00044 Frascati (RM), Italy
[12] INAF—Osservatorio Astronomico di Roma, 00078 Monte Porzio Catone (RM), Italy
Received 2025 September 5; revised 2025 September 25; accepted 2025 September 26; published 2025 October 16

Abstract

We present the first polarimetric observations of the third discovered interstellar object (ISO), 3I/ATLAS (C/2025 N1, or 3I), obtained preperihelion with FORS2 at the Very Large Telescope, ALFOSC at the Nordic Optical Telescope, and FoReRo2 at the 2 m Ritchey-Chrétien-Coudé telescope, over a phase angle range of 7.°7–22.°4. This marks the second-ever polarimetric study of an ISO, the first distinguishing 2I/Borisov from most solar system comets by its higher positive polarization. Our polarimetric measurements as a function of phase angle reveal that 3I is characterized by a deep and narrow negative polarization branch, reaching a minimum value of −2.7% at phase angle 7°, and an inversion angle of 17°—a combination unprecedented among asteroids and comets, including 2I/Borisov. At very small phase angles, the extrapolated slope of the polarization phase curve is consistent with that of certain small trans-Neptunian objects and Centaur Pholus, consistent with independent spectroscopic evidence for a red, possibly water-ice-bearing object. Imaging confirms a diffuse coma present from our earliest observations, though no strong polarimetric features are spatially resolved. These findings may demonstrate that 3I represents a distinct type of comet, expanding the diversity of known interstellar bodies.

Unified Astronomy Thesaurus concepts: Interstellar objects (52); Polarimetry (1278)

1. Introduction

The object 3I/ATLAS (C/2025 N1, initially designated A11pl3Z; hereafter referred to as 3I) was discovered by the ATLAS survey on 2025 July 1 and was quickly recognized to follow a retrograde, hyperbolic orbit with an eccentricity of ∼6 and an inclination exceeding 175°, securely establishing its extrasolar origin (D. Z. Seligman et al. 2025). It is only the third interstellar object (ISO) discovered to date, after 1I/'Oumuamua (hereafter 1I) and 2I/Borisov (hereafter 2I). The first two ISOs displayed radically different physical properties: 1I (discovered in 2017), an unexpectedly red, elongated, tumbling object, displayed nongravitational accelerations without detectable activity despite deep searches (e.g., K. J. Meech et al. 2017; M. Micheli et al. 2018), while 2I (discovered in 2019) was an active comet with gas species and dust properties broadly consistent with solar system comets, though with an unusually high CO abundance (e.g., P. Guzik et al. 2020; C. Opitom et al. 2021) and atypical polarimetric properties (S. Bagnulo et al. 2021). Thus, with 1I appearing asteroid-like but enigmatic and 2I mostly resembling a familiar comet, the arrival of 3I offers the possibility of sampling yet another member of the diverse ISO population and of testing whether its dust and activity reflect known objects or not. Due to their hyperbolic orbits, ISOs only appear for a single passage through the solar system; capture into a bound orbit (T. O. Hands & W. Dehnen 2020; W. Dehnen et al. 2022) or reencounter with the Sun where a second orbit may be observed are extremely unlikely possibilities. Hence, the time between an ISO's discovery and its last observable moment postperihelion is the critical period for characterizing an ISO.

Multitechnique observations—including astrometry, photometry, and spectroscopy—are being used to refine 3I's orbit, detect volatile outgassing, and characterize the dust and gas components of the coma for direct comparison with typical solar system objects. Early results show that 3I is quite red, similar to D-type asteroids, most likely due to an active dust coma in the absence of volatile gas sublimation near its discovery (M. Belyakov et al. 2025; B. T. Bolin et al. 2025; C. O. Chandler et al. 2025; T. Kareta et al. 2025; C. Opitom et al. 2025; D. Z. Seligman et al. 2025). Unsurprisingly, 3I hence displays little lightcurve variability (C. O. Chandler et al. 2025; R. de la Fuente Marcos et al. 2025; T. Kareta et al. 2025; T. H. Puzia et al. 2025; D. Z. Seligman et al. 2025). Kinematic analysis of its inbound velocity compared to the expected velocity distribution of the Galactic population suggest an origin distinct from either 1I or 2I, likely originating in an older, lower-metallicity star system (R. de la Fuente Marcos et al. 2025;

M. J. Hopkins et al. 2025; A. G. Taylor & D. Z. Seligman 2025). Specifically, M. J. Hopkins et al. (2025) predicted that 3I would likely become more active closer to the water-ice line due to an estimated large fraction of mass as water; a prediction supported by recent indirect and direct detections of water-ice emission (Z. Xing et al. 2025; B. Yang et al. 2025) at atypically large heliocentric distances $r_h \geqslant 3.51$ au. IR observations by the JWST at $r_h = 3.3$ au reveal a CO_2 dominated coma, with a CO_2/H_2O mixing ratio among the highest ever recorded at such a heliocentric distance, as well as the presence of H_2O, CO, OCS, water ice, and dust (M. A. Cordiner et al. 2025). While already displaying similar cometary characteristics to 2I, 3I is the largest ISO ever discovered, with Hubble Space Telescope observations constraining its radius to $0.22 \leqslant r \leqslant 2.8$ km (D. Jewitt et al. 2025), assuming an albedo $\rho_V = 0.04$. The detailed characterization of 3I currently ongoing by the astronomical community is vital for informing our expectations of interstellar asteroids and comets from different origins within the galaxy, as well as placing 1I and 2I into the context of the broader ISO population (E. G. Flekkøy & R. Toussaint 2023).

While spectroscopy and imaging help constrain composition and morphology, polarimetry uniquely probes physical properties of the object—such as optical constants, grain size distribution, and dust shape and structure in the case of a cometary coma or surface regolith—that are not easily inferred from other techniques. The degree of linear polarization P_r of sunlight scattered by cometary dust particles is measured as the difference between the fluxes perpendicular and parallel to the scattering plane (Sun–comet–observer plane), normalized by their sum, and is highly sensitive to the solar phase angle α (Sun–comet–observer angle). Because of this definition, polarization is positive when the polarization direction is oriented perpendicular to the scattering plane, and negative when parallel. Overall, solar system objects show similar phase angle dependence $P_r(\alpha)$: negative polarization at small phase angles ($\alpha \lesssim 20^\circ$) and positive at larger phase angles, increasing nearly linearly until reaching a maximum at $\alpha \simeq 90^\circ$–100°. The detailed shape of this curve varies according to each object: the minimum and maximum values of polarization (P_{max} and P_{min}), their corresponding phase angles (α_{max} and α_{min}), the so-called inversion angle α_0 where the polarization switches sign, and the slope of the curve at this angle $h = \Delta P/\Delta\alpha$. Combined with photometric and spectroscopic data, these six parameters provide a framework for theoretical studies to constrain the physical properties of the scattering media. For example, using large porous particles with highly absorbing inclusions in a laboratory setting, O. Muñoz et al. (2020) were able to reproduce both the OSIRIS/Rosetta phase function and polarimetric phase curve obtained via ground-based observations of comet 67P/Churyumov–Gerasimenko.

In the case of cometary atmospheres, dust properties (hence, polarization) can vary throughout a comet's apparition according to heliocentric distance r and cometocentric distance ρ (and therefore, aperture radius). Despite accounting for these variables, consistent trends still emerge. Studies show that most comets generally fall into one of two broad polarimetric classes defined by their P_{max} values: high-polarization comets, with $P_{max} \simeq 25\%$–30% at $\alpha_{max} \simeq 95^\circ$; and low-polarization comets, with $P_{max} \simeq 8\%$–22% at $\alpha_{max} \simeq 90^\circ$ (N. Kiselev et al. 2015). A handful of exceptional objects deviate significantly from these classes. The best-known case is C/1995 O1 (Hale–Bopp), which shows polarization values about 4% higher than typical high-polarization comets at phase angles $\gtrsim 35^\circ$, leading to the definition of a distinct "Hale–Bopp-like" polarimetric class (E. Hadamcik & A. C. Levasseur-Regourd 2003). For many years, Hale–Bopp remained unique in this regard, until the appearance of 2I. Very Large Telescope (VLT) polarimetric observations of 2I by S. Bagnulo et al. (2021) revealed a phase dependence remarkably similar to that of Hale–Bopp, despite spectroscopic and photometric studies finding it otherwise consistent with typical solar system comets. These data thus established 2I as the first ISO with polarimetric measurements, and placed it in the exceptional Hale–Bopp class.

The arrival of 3I provides a new opportunity to extend such studies. In this Letter, we present the first polarimetric observations of 3I that probe the poorly explored negative polarization branch of an ISO.

2. Observations and Analysis

We obtained 18 preperihelion imaging polarimetric observations of 3I using three different instruments between 2025 July 17 and August 28 corresponding to a phase angle range of $7.^\circ7$–$22.^\circ4$ and heliocentric distance range of 4–2.6 au. Observations were conducted in the *R* band using FORS2 at the ESO VLT (8.2 m), ALFOSC at the Nordic Optical Telescope (NOT; 2.56 m), and FoReRo2 at the 2 m Ritchey–Chrétien-Coude (RCC), while three additional *V*-band observations were acquired with FORS2. A summary of the observing log is presented in Table 1. We obtained one earlier observation with ALFOSC on 2025 July 11 (at phase angle $5.^\circ7$) but were unable to obtain a reliable measurement due to the dense star field at the time of the observation.

For the analysis of our data, we performed aperture polarimetry using a ∼2000 km radius circular aperture centered on the photocenter. We opted for this small aperture size to avoid contamination from background field stars, of which there were many in the earliest epochs. This aperture method is useful for comparing the bulk properties of 3I to those of other objects, but loses spatial information due to the averaging of integrated signal within the aperture. We overcame this issue by constructing polarimetric maps and deep imaging maps from our FORS2 data. Full details of the data reduction procedures for these instruments are provided, for example, in Z. Gray et al. (2024a, 2024b) and G. Borisov et al. (2015). We outline the basic principles in Appendices A and B.

3. Results

3.1. Aperture Polarimetry

The values of the linear polarization measurements at each epoch are listed in Table 1 and plotted as a function of phase angle in Figure 1, together with data for various solar system bodies. Our observations show that 3I exhibits expected polarimetric behavior, showing negative polarization at small phase angles and a linear increase of polarization with increasing phase angle. In order to compare 3I to other objects, we fit the linear-exponential empirical model suggested by K. Muinonen et al. (2009) to the data:

$$P_r(\alpha) = A(e^{-(\alpha/B)} - 1) + C\,\alpha, \quad (1)$$

where α is the phase angle, and A, B, and C are free parameters that shape the curve. The best-fit parameters of 3I are given in Table 2.

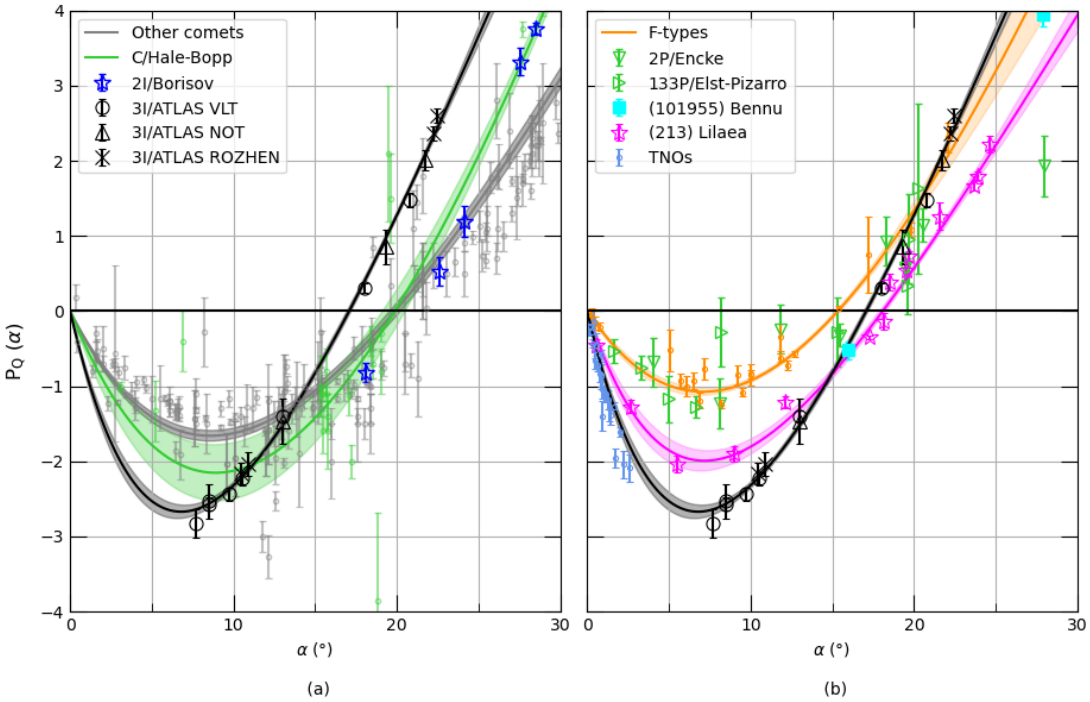

Figure 1. Polarization vs. phase angle of 3I compared to various other objects. Solid lines with shaded areas represent best-fit curves calculated according to Equation (1) with $\pm 1\sigma$ uncertainty. Left: "other comets" represents several solar system comets, including both periodic comets (e.g., 9P/Tempel 1, 22P/Kopff, 47P/Ashbrook–Jackson, 67P/Churyumov–Gerasimenko) and nonperiodic comets (e.g., C/2000 WM1 (LINEAR), C/2009 P1 (Garradd)), sourced from the Database of Comet Polarimetry (N. Kiselev et al. 2017). Right: F-type curve is calculated using (302) Clarissa, (419) Aurelia, and (704) Interamnia data, sourced from the Asteroid Polarimetric Database (D. Lupishko 2019); trans-Neptunian object (TNO) data points include Huya, Ixion, 1999 DE9, and Varuna, as well as Centaur Pholus, sourced from the TNO Polarimetric Database (I. N. Belskaya 2013). The 3I data in the right image are as labeled in the left. All other data points are as labeled in the legends. All data are in *R* band, except for (213) Lilaea, for which only *V*-band data exist.

Table 1
Results of Aperture Polarimetric Measurements of 3I Using Aperture Radius of Approximately 2000 km

Date	UT	Instrument	α (deg)	r (au)	Wave Band	P_Q (%)	P_U (%)
2025 Jul 17	01:30	FORS2	7.7	3.98	*R*	-2.83 ± 0.19	0.12 ± 0.24
2025 Jul 17	01:54	FORS2	7.7	3.98	*V*	-2.72 ± 0.16	...
2025 Jul 18	23:57	FORS2	8.5	3.92	*R*	-2.53 ± 0.23	0.18 ± 0.26
2025 Jul 19	00:19	FORS2	8.5	3.92	*V*	-2.87 ± 0.14	...
2025 Jul 19	00:51	FORS2	8.5	3.92	*R*	-2.57 ± 0.09	...
2025 Jul 22	00:09	FORS2	9.7	3.82	*R*	-2.44 ± 0.08	...
2025 Jul 23	20:35	FoReRo2	10.5	3.76	*R*	-2.17 ± 0.14	...
2025 Jul 24	00:37	FORS2	10.5	3.75	*R*	-2.23 ± 0.09	...
2025 Jul 24	21:00	FoReRo2	10.8	3.73	*R*	-2.03 ± 0.16	...
2025 Jul 29	22:27	ALFOSC	13.0	3.56	*R*	-1.46 ± 0.30	0.01 ± 0.30
2025 Jul 30	00:49	FORS2	13.0	3.56	*R*	-1.40 ± 0.07	...
2025 Aug 12	00:22	FORS2	18.0	3.14	*R*	0.30 ± 0.07	...
2025 Aug 15	21:37	ALFOSC	19.3	3.01	*R*	0.86 ± 0.23	-0.26 ± 0.23
2025 Aug 21	02:16	FORS2	20.8	2.85	*R*	1.48 ± 0.10	-0.18 ± 0.10
2025 Aug 21	02:27	FORS2	20.8	2.85	*V*	1.15 ± 0.11	...
2025 Aug 24	21:12	ALFOSC	21.7	2.73	*R*	2.18 ± 0.14	0.01 ± 0.14
2024 Aug 27	18:45	FoReRo2	22.3	2.64	*R*	2.37 ± 0.10	0.03 ± 0.10
2024 Aug 28	18:25	FoReRo2	22.4	2.61	*R*	2.59 ± 0.10	0.23 ± 0.10

Note. In cases where a P_U value is missing, this implies that the instrument position angle is already rotated to the scattering plane—see Appendix A.

According to our *R*-band data, 3I is characterized by an inversion angle of $\alpha_0 = 17.^\circ1 \pm 0.^\circ1$—a particularly small value compared to the typical value of 20°–22° of solar system comets, as well as that of the Hale–Bopp-like group to which 2I belongs (characterized by $\alpha_0 \simeq 20.^\circ5$). With values $P_{\rm min} = -2.7\%$ at $\alpha_{\rm min} = 7^\circ$, the negative polarization branch of 3I is notably deeper and shifted to smaller phase angles than that observed for these comet classes, as shown in Figure 1(a). The slope at the inversion angle is another key diagnostic parameter, with empirical studies showing that asteroids exhibit a direct correlation between slope and geometric albedo known as Umov's law (B. Zellner & J. Gradie 1976;

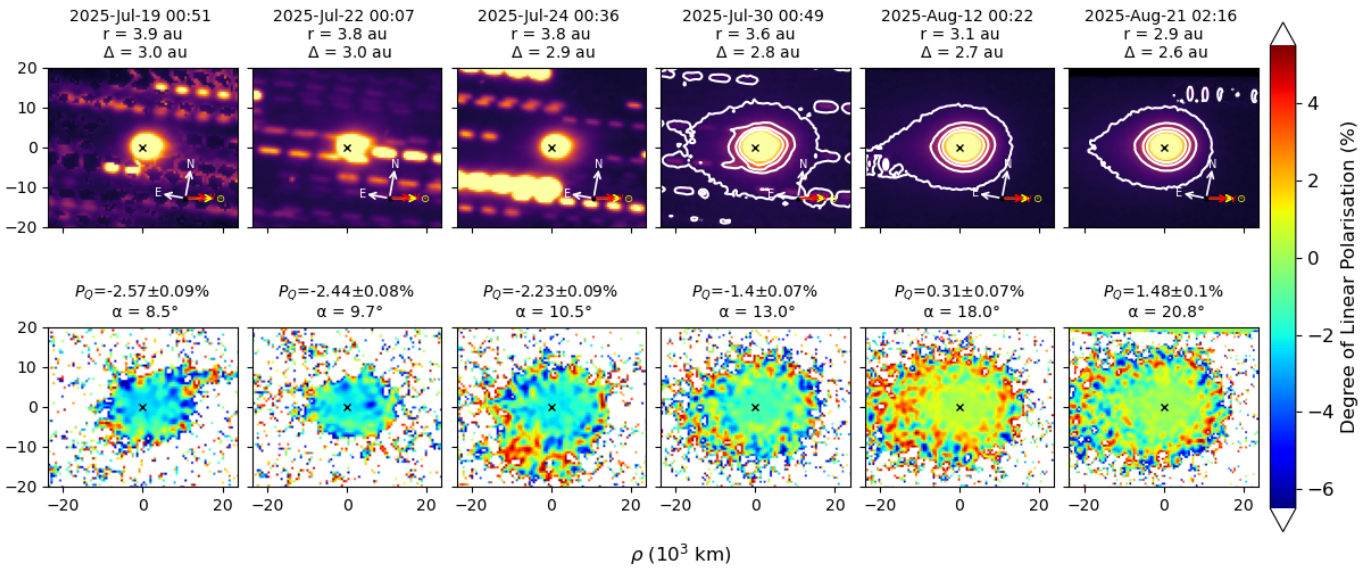

Figure 2. Deep imaging (top) and polarimetric (bottom) maps of 3I from a subset of VLT observations (*R* band). The color scale in the imaging maps does not reflect the absolute brightness of the comet. We display isophotes in the last three epochs only due to the large number of background stars in the first images. The color of each pixel in the polarimetric maps represents the value of polarization, as shown in the scale to the right. Pixels with values outside this color scale are given in white and are considered noise. The arrows indicate the directions toward the celestial north and east, as well as the Sun–comet direction and velocity direction of the comet (which mostly overlap) projected onto the sky. X marks the comet photocenter.

Table 2
R-band Polarimetric Phase Curve Parameters of 3I According to the Best-fit Model

Object	$P_{\min}$ (%)	$\alpha_{\min}$ (deg)	α_0 (deg)	h (% deg^{-1})
3I/ATLAS	−2.67 ± 0.08	6.79 ± 1.34	17.08 ± 0.12	0.416 ± 0.008

A. Cellino et al. 2015); the steeper the slope, the lower the albedo. From our 3I curve, we measure a polarimetric slope of $h = 0.42\%$ deg^{-1}, a value somewhat extreme among the typical 0.2–0.4% deg^{-1} range for solar system comets, but comparable to the 0.45% deg^{-1} slope of 2I. If 3I were an asteroid or we were observing the comet nucleus directly, such a slope would correspond to an extremely low albedo ($\rho_V \simeq 0.04$). However, the empirical albedo-polarization slope relationship used for asteroids cannot be strictly applied to cometary comae due to the difference in light-scattering physics between densely packed particulate surfaces compared to diffuse particulate clouds (E. Zubko et al. 2011). Regardless, the combination of such a shallow inversion angle and deep negative polarization branch is unprecedented among comets observed to date.

3.2. Imaging Polarimetry

Figure 2 presents *R*-band deep imaging and polarimetric maps for a subset of our FORS2 data. For the last three epochs, we overlap isophotes to highlight the morphology of the extended coma, but we omit them in the first three images due to the high density of background stars. In these early frames, the photocenter of 3I passes close to several field stars, illustrating the rationale for adopting a small aperture for the aperture polarimetric measurements. We verified that this aperture was sufficiently small to avoid contamination from the background stars—i.e., while the polarimetric map of the extended coma in the July 22 epoch (in the projected direction south of the photocenter) is affected by a nearby star, we remain confident that our aperture polarimetric measurement remains intact. We include these maps despite the dense star field for completeness.

A weak diffuse coma is apparent from our earliest data sets, which grew steadily as the heliocentric distance decreased with time. No clear tail was visible at these early epochs—it was likely projected behind the comet, hidden from our point of view due to the observing geometry—but it later emerged as an extension of the coma in the antisolar direction. The absence of a prominent tail in early observing epochs is consistent with reports, for example, by T. Kareta et al. (2025) and T. Santana-Ros et al. (2025). The polarimetric maps reveal no significant spatial structures or variations across the coma and tail. This is in line with recent polarimetric studies of other comets, including 2I (S. Bagnulo et al. 2021), Oort-cloud comet C/2017 K2 (PANSTARRS; Y. G. Kwon et al. 2024), and Jupiter Family Comet 67P/Churyumov–Gerasimenko (Z. Gray et al. 2024a). Continued monitoring of 3I with imaging and polarimetric mapping in future epochs will be crucial to track the evolution of its coma and better understand its dust properties and activity in comparison to other comets.

4. Discussion

The inversion and minimum angles of 3I approach those of classic F-type asteroids ($\alpha_0 \simeq 15°$, $\alpha_{\min} \simeq 7°$) as defined by J. Gradie & E. Tedesco (1982). Though limited, polarimetric observations of cometary nuclei, namely 2P/Encke (D. Jewitt 2004; H. Boehnhardt et al. 2008) and 133P/Elst–Pizarro (S. Bagnulo et al. 2010), likewise show low inversion angles similar to that of F-type asteroids. Moreover, (4015) Wilson–Harrington, an object originally classified as an F-type asteroid upon its discovery (E. Bowell et al. 1992), was later found to exhibit cometary activity. A lack of further activity detections in subsequent observations, however, suggests that Wilson–Harrington may be a comet becoming extinct.

Intriguingly, more recent work has strengthened this connection: (101955) Bennu, the target of the OSIRIS-REx sample return mission, was found to display F-type-like polarimetric properties (A. Cellino et al. 2018) despite previously being classified as a B-type according to the S. J. Bus & R. P. Binzel (2002) taxonomic classification system. Analysis of the first data collected in situ by the spacecraft later revealed that Bennu is a low-albedo asteroid with a surface rich in hydrated minerals and with moderate surface activity, and even with evidence of past water flow within the asteroid (C. W. Hergenrother et al. 2020; K. Ishimaru & D. S. Lauretta 2024), reinforcing the idea of a possible cometary nature of members of the F-class. Another recent, interesting example is that of asteroid 25330 (1999 KV4), which shows extremely high polarization at large phase angles, almost coinciding with the phase curve of Hale–Bopp at angles 30°–50° (M. P. Shcherbina et al. 2025), and sharing a similar inversion angle to 3I. These pieces of evidence suggest an inherent link between F-type asteroids and cometary nuclei, and thus it has been proposed that a low inversion angle could be diagnostic of a cometary surface (e.g., H. Boehnhardt et al. 2008; M. Devogèle et al. 2018).

Some known asteroids illustrate that a low inversion angle does not always coincide with the typical, moderate depth of the negative branch seen in F-type asteroids. For example, (213) Lilaea, originally classified as F-type based on albedo and spectrophotometric data, is characterized by polarization phase curve parameters $\alpha_0 \simeq 18.^{\circ}1$, $\alpha_{\min} \simeq 7.^{\circ}1$, and $P_{\min} \simeq -2\%$—a negative polarization branch roughly twice as deep as that of typical F types, as shown in Figure 1(b). In contrast, (269) Justitia (not listed in the figure to avoid overcrowding) exhibits $\alpha_0 \simeq 15°$, $\alpha_{\min} \simeq 6.^{\circ}5$, and $P_{\min} \simeq -0.6\%$—about half the typical depth (R. Gil-Hutton et al. 2014). Spectral studies of (269) Justitia reveal an unusually steep red slope, redder than that of D-type asteroids, and closer to that of some trans-Neptunian objects (TNOs; S. Hasegawa et al. 2021, 2022; O. A. Humes et al. 2024). The peculiarity of this particular object has also been noted by A. Cellino et al. (2020) and M. Mahlke et al. (2022), with the latter assigning (269) Justitia to the rare and relatively new Z-type taxonomic class. Overall, these examples suggest that objects with inversion angles around 15° often prove to be anomalous and intrinsically interesting cases, worthy of further study.

Despite sharing a small inversion angle with these unique cases, the depth of 3I's negative polarization branch still sets it apart entirely. We report the first clear example of a planetary body whose polarimetric behavior is dominated by such a deep and narrow negative polarization branch. Such behavior has never been observed among solar system objects: not in comets, which typically show shallower negative branches and larger inversion angles, nor in asteroids, even those belonging to rare and unusual taxonomic classes.

At very small phase angles ($\alpha \leqslant 2°$), the extrapolated fit of 3I most closely resembles the steep polarization curves observed for small TNOs (diameters 310–670 km), Huya, Ixion, Varuna, and 1999 DE_9, as well as Centaur Pholus (S. Bagnulo et al. 2006; I. N. Belskaya et al. 2010; see Figure 1(b)). These objects, only observable at small phase angles from ground-based observatories, are characterized by an extremely rapid increase in polarization (absolute value), showing a much steeper slope at $\alpha = 0°$–$2°$ compared to other objects. It is worth noting, however, that this polarimetric behavior is not universal among all TNOs and Centaurs—most other objects show much slower variations in polarization with phase angle. The common trait among these four TNOs is a deeper negative branch compared to larger and methane-rich TNOs, as well as belonging to the same IR taxonomic class (M. Fulchignoni et al. 2008) showing moderately red, featureless, visible to near-IR spectra with weak to strong detections of water ice (A. Alvarez-Candal et al. 2007; M. A. Barucci et al. 2011).

The similarity between 3I's steep polarimetric slope at small phase angles and that of certain TNOs is in line with independent spectroscopic and color measurements that show that 3I appears redder than solar system comets and D-type asteroids (A. Alvarez-Candal et al. 2025; B. T. Bolin et al. 2025; R. de la Fuente Marcos et al. 2025; C. Opitom et al. 2025; T. Santana-Ros et al. 2025), possibly closer to the surfaces of some TNOs and Centaurs. Further, the predicted presence of water ice (M. J. Hopkins et al. 2025) was detected both indirectly and directly via spectroscopic measurements (Z. Xing et al. 2025; B. Yang et al. 2025).

Among theoretical studies, numerical simulations suggest that the observed polarimetric behavior of TNOs and Centaurs arises from a surface mixture of bright and dark scatterers, and that the different polarimetric behaviors (i.e., fast and slow variation with phase angle) among TNOs and Centaurs can be explained via different ratios of these scatterers (e.g., S. Bagnulo et al. 2006; I. N. Belskaya et al. 2008). Laboratory studies show that even small amounts of bright grains added to dark powders significantly enhance negative polarization (A.-C. Levasseur-Regourd et al. 2015). In particular, laboratory experiments by L. M. Dougherty & J. E. Geake (1994) and O. Poch et al. (2018) demonstrate that thin frost layers of water ice on dark surfaces produce deep minima shifted toward small phase angles, together with a reduced inversion angle—closely resembling the behavior observed for some TNOs and 3I. Of course, in the case of 3I, our polarization measurements are not probing the consolidated regolith surface but rather a diffuse coma of dust and ice grains. Interestingly, L. M. Dougherty & J. E. Geake (1994) found a similar minimum at small phase angles, but with reduced depth, together with a small inversion angle when repeating the experiments for a diffuse cloud of water-ice particles over a dark surface. Light-scattering models of large cometary particles by O. Ivanova et al. (2023) show that reproducing a deep polarization minimum requires the inclusion of ice particles in highly porous particles. Their model, which treats grains as aggregates of submicron monomers with silicate-organic cores (50/50 mixture) and water- and CO_2-ice mantles (90/10 mixture), demonstrates that both particle size and porosity play key roles in shaping the polarimetric phase curves: larger particles shift $\alpha_{\min}$ toward smaller phase angles (see also E. Frattin et al. 2022), while $P_{\min}$ (absolute value) increases with porosity but exhibits nonlinear dependence on particle size. With these studies in mind, the extreme depth of the negative polarization branch of 3I hints at a mixture of icy and dark material, though the exact properties of the particles are still uncertain. The picture may become clearer with further observations as well as theoretical studies combining polarimetry with results from other observational techniques.

We caution that the comparison between 3I and TNOs remains tentative. Our measurements of $P_{\min}$ and $\alpha_{\min}$ correspond to the upper limit only since our data do not show the expected turnover toward zero polarization for small phase angles. Further, the lack of data at $\alpha < 7°$ for 3I and $\alpha > 2°$ for TNOs makes a full comparison difficult. Observations of 3I after perihelion, when it will be visible in the phase angle

range $\sim 0^\circ$–30°, will be critical to confirm its polarimetric behavior at small phase angles and explore the genuineness of the parallels with that of TNOs and Centaurs.

5. Summary and Conclusions

In this Letter, we present preperihelion imaging polarimetric observations of the third discovered interstellar comet, 3I/ATLAS. Our measurements establish 3I as uniquely distinct, compared to both solar system bodies and 2I, the only other ISO observed polarimetrically.

3I is characterized by an extremely deep and narrow negative polarization branch, with parameters $P_{\rm min} = -2.67\% \pm 0.08\%$, $\alpha_{\rm min} = 6.^\circ 79 \pm 1.^\circ 34$, $\alpha_0 = 17.^\circ 08 \pm 0.^\circ 12$, and $h = 0.42 \pm 0.01\%$ deg^{-1}. This polarimetric behavior is different from all known comets (either interstellar or bound to our solar system), not fitting into either the high- or low-polarization comet categories, nor that of the unique category occupied by just Hale–Bopp and 2I. While 3I's inversion angle resembles that of rare F-type asteroids and cometary nuclei, the depth of its negative polarization branch is almost twice as large. Extrapolation to very small phase angles indicates a steep polarization slope between phase angles 0°–2°, reminiscent of certain small TNOs and Centaurs. While this finding is tentative due to a lack of data at small phase angles, it is consistent with the red spectral slope and evidence of water-ice detections in various independent studies.

Imaging confirms the presence of a diffuse coma present from the earliest epochs that grows steadily with decreasing heliocentric distance. Our polarimetric maps reveal no significant spatial variations, suggesting homogeneous polarization of the coma. Thus, our polarimetric measurements most likely probe the dust in the coma rather than the nucleus surface (in agreement with D. Jewitt et al. 2025, at a similar epoch). Direct comparisons to atmosphereless bodies must be made with caution since the underlying light-scattering physics differ fundamentally. Still, we explore 3I's similarity to all types of solar system objects for completeness as our knowledge of the object continues to evolve. Based on theoretical studies of cometary particles (O. Ivanova et al. 2023), the depth of the negative branch and small $\alpha_{\rm min}$ value for 3I hints at the presence of large particles composed of a mixture of icy and dark material.

Overall, the combination of low inversion angle and extreme negative polarization is unprecedented among comets and asteroids, marking 3I as the first object known with such polarimetric behavior and possibly representing a previously unobserved class of small planetary bodies. Its polarimetric characteristics provide novel insights into the dust properties of ISOs, suggesting that ISOs may encompass a broader diversity than previously recognized. Further postperihelion observations in the coming months, when 3I will be visible between phase angles $\sim 0^\circ$–30° and heliocentric distance < 2 au, will be critical for fully characterizing its polarimetric behavior and confirming the parallels (or lack thereof) with known solar system bodies, as well as constraining its particle properties based on laboratory and computational studies.

Acknowledgments

Based on observations obtained with the FORS2 instrument at the ESO Telescopes at the La Silla Paranal Observatory under program ID 115.29F8.001, 115.29F8.002, 115.29F8.003, 115.29F8.004, 115.29F8.005 (PI Bagnulo). Based on observations made with the Nordic Optical Telescope, owned in collaboration by the University of Turku and Aarhus University, and operated jointly by Aarhus University, the University of Turku and the University of Oslo, representing Denmark, Finland, and Norway, the University of Iceland, and Stockholm University at the Observatorio del Roque de los Muchachos, La Palma, Spain, of the Instituto de Astrofisica de Canarias. The NOT data were obtained under program ID P71-413 (PI Fedorets). The data presented here were obtained in part with ALFOSC, which is provided by the Instituto de Astrofisica de Andalucia (IAA) under a joint agreement with the University of Copenhagen and NOT. Based on observations obtained at BNAO Rozhen during semester 2025A under the program "Investigation of the physicochemical properties of different classes of comets" led by G. Borisov. All FORS2 raw data and calibrations are available at archive.eso.org.

Z.G., A.P., and K.M. acknowledge support by the Research Council of Finland (grants #359893 and #336546).

R.C.D. and M.G. acknowledge support from grant #361233 awarded by the Research Council of Finland.

G.B. acknowledges partial support from grant КП-06-H88/5 by the Bulgarian National Science Fund.

G.B. gratefully acknowledges observing grant support from the Institute of Astronomy and National Astronomical Observatory, Bulgarian Academy of Sciences.

Open access funded by Helsinki University Library.

Appendix A
Instrumental Setup and Observing Strategy

Imaging polarimetric observations were obtained in the R and V bands using three instruments: FOcal Reducer/low dispersion Spectrograph (FORS2) at the 8.2 m VLT of the European Southern Observatory (ESO; Chile), Alhambra Faint Object Spectrograph and Camera (ALFOSC) at the 2.56 m NOT in Roque de Los Muchachos (La Palma, Spain), and the two-channel Focal Reducer Rozhen (FoReRo2) at the RCC telescope of the Bulgarian National Astronomical Observatory (BNAO) Rozhen. The filters used and their central wavelength (λ_c) and FWHM are the following: FORS2 broadband filters R_SPECIAL ($\lambda_c = 655$ nm, FWHM = 165 nm) and v_HIGH ($\lambda_c = 557$ nm, FWHM = 123.5 nm); ALFOSC broadband filter R_BES 641_148 ($\lambda_c = 641$ nm, FWHM = 148 nm); and FoReRo2 narrowband filter Rx ($\lambda_c = 694$ nm, FWHM = 79 nm). We abbreviate these wave bands as R and V bands. The transmission curve of each filter is given in Figure 3.

The polarimetric optics of all three instruments follow the design suggested by I. Appenzeller (1967): a rotatable retarder wave plate followed by a beam-splitting device. This arrangement produces ordinary and extraordinary beams separated (by $22''$, $15''$, and $62.''5$ for FORS2, ALFOSC, and FoReRo2, respectively) on the detector, allowing for simultaneous measurement of orthogonally polarized intensities.

By taking observations consisting of a series of exposures with the $\lambda/2$ retarder wave plate set at position angles $\delta = 0^\circ$, $22.^\circ 5$, 45°, …, $337.^\circ 5$, or a subset of these angles, we measured the degree of linear polarization using the so-called beam-swapping technique described in S. Bagnulo et al. (2009). If $f^{\parallel}$ and $f^{\perp}$ are the fluxes measured in the parallel and perpendicular beams, respectively, we calculate the reduced Stokes parameters

Table 3
3I/ATLAS Observing Log

Date	UT	Instr.	α (deg)	r (au)	Δ (au)	Φ (deg)	PA (deg)	Wave Band	Exp (s)	n_Q	n_U
2025 Jul 17	01:30	FORS2	7.7	3.98	3.08	100.9	11.0	*R*	6 x 70	4	2
2025 Jul 17	01:54	FORS2	7.7	3.98	3.08	100.9	11.0	*V*	6 x 100	6	0
2025 Jul 18	23:57	FORS2	8.5	3.92	3.04	100.6	11.0	*R*	8 x 70	6	2
2025 Jul 19	00:19	FORS2	8.5	3.92	3.04	100.6	11.0	*V*	6 x 100	6	0
2025 Jul 19	00:51	FORS2	8.5	3.92	3.04	100.6	10.5	*R*	8 x 50	8	0
2025 Jul 22	00:09	FORS2	9.7	3.82	2.98	100.2	10.2	*R*	6 x 90	6	0
2025 Jul 23	20:35	FoReRo2	10.5	3.76	2.94	100.1	0	*R*	12 x 300	6	6
2025 Jul 24	00:37	FORS2	10.5	3.75	2.94	100.1	10.1	*R*	6 x 60	6	0
2025 Jul 24	21:00	FoReRo2	10.8	3.73	2.93	100.1	0	*R*	24 x 300	12	12
2025 Jul 29	22:27	ALFOSC	13.0	3.56	2.84	100.1	90.0	*R*	16 x 100	8	8
2025 Jul 30	00:49	FORS2	13.0	3.56	2.84	100.1	10.1	*R*	6 x 80	6	0
2025 Aug 12	00:22	FORS2	18.0	3.14	2.69	101.1	10.8	*R*	8 x 40	8	0
2025 Aug 15	21:37	ALFOSC	19.3	3.01	2.66	101.5	90.0	*R*	16 x 80	8	8
2025 Aug 21	02:16	FORS2	20.8	2.85	2.62	102.0	11.8	*R*	8 x 30	4	4
2025 Aug 21	02:27	FORS2	20.8	2.85	2.62	102.0	11.8	*V*	4 x 40	4	0
2025 Aug 24	21:12	ALFOSC	21.7	2.73	2.60	102.3	90.0	*R*	16 x 80	8	8
2025 Aug 27	18:45	FoReRo2	22.2	2.64	2.59	102.6	0	*R*	8 x 300	4	4
2025 Aug 28	18:25	FoReRo2	22.4	2.61	2.59	102.7	0	*R*	8 x 300	4	4

Note. α is the phase angle, r is the heliocentric distance, Δ is the geocentric distance, Φ is the position angle of the scattering plane, PA is the position angle of the instrument (counted positive N to E), and n_Q and n_U are the numbers of frames used to calculate P_Q and P_U, respectively. In cases where a column/row parameter is not listed, its value is equal to that in the previous row.

$P'_Q = Q/I$ and $P'_U = U/I$ (W. A. Shurcliff 1962) as

$$P'_X = \frac{1}{2N}\sum_{j=1}^{N}\left[\left(\frac{f^{\parallel} - f^{\perp}}{f^{\parallel} + f^{\perp}}\right)_{\delta=\delta_j} - \left(\frac{f^{\parallel} - f^{\perp}}{f^{\parallel} + f^{\perp}}\right)_{\delta=\delta_j+45^\circ}\right], \quad \text{(A1)}$$

where $\delta_j \in \{0^\circ, 90^\circ, 180^\circ, 270^\circ\}$ for $X = Q$; and $\delta_j \in \{22.^\circ 5, 112.^\circ 5, 202.^\circ 5, 295.^\circ 5\}$ for $X = U$, and N is the number of pairs of exposures per Stokes parameter. The number of frames used to calculate each Stokes parameter in each epoch is given in Table 3. We then transform these Stokes parameters to the direction perpendicular to the scattering plane using

$$P_Q = P'_Q \cos(2\chi) + P'_U \sin(2\chi)$$
$$P_U = -P'_Q \sin(2\chi) + P'_U \cos(2\chi), \quad \text{(A2)}$$

where $\chi = \mathrm{PA} + \Phi + 90^\circ + \epsilon(\lambda)$. Here, PA is the position angle of the instrument (the direction of the principal plane of the beam splitter) counted counterclockwise from the great circle passing through the comet and the north celestial pole, Φ is the position angle of the scattering plane (comet–Sun direction relative to comet–north celestial pole direction), and $\epsilon(\lambda)$ is the wavelength-dependent chromatism correction angle of the retarder wave plate.

Regarding observing strategy, we adjusted the PA angle in two distinct ways to accommodate the characteristics of the instruments. In the case of ALFOSC, we rotated the PA to avoid overlap between the extended coma/tail and the photocenter in the $f^{\parallel}$ and $f^{\perp}$ beams, estimating the expected direction of the tail in advance using the Φ angle together with the comet's heliocentric velocity vector (listed as PsAng and PsAMV by JPL Horizons). Since both of these values remained close to 90° throughout all observations, a simple PA rotation of 90° was sufficient. In addition to this, we ensured there was no overlap despite the rotation via visual inspections and numerical tests.

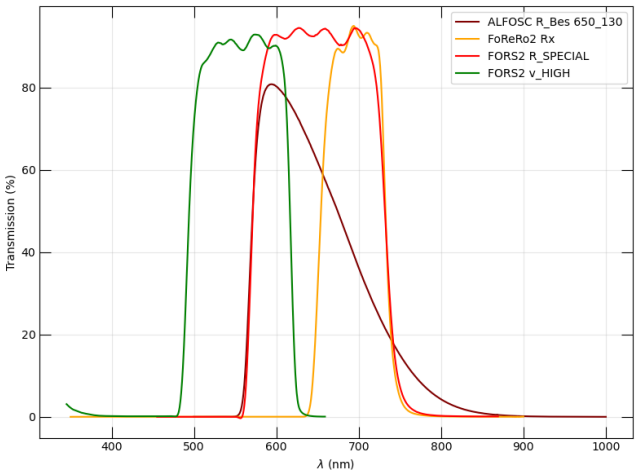

Figure 3. Transmission curves of *R*- and *V*-band filters used for observations.

For FORS2, this overlap is not an issue thanks to an additional optical element, the strip mask (Wollaston mask): this is composed of strips of opaque material of width equal to the $f^{\parallel} - f^{\perp}$separation, preventing the superposition of the two images. The resulting image appears as $6.'8 \times 22''$ strips of double images, i.e., the ordinary and extraordinary beams neatly separated without overlap, though with the disadvantage of a vignetted field of view. In this case, for most observations, we instead rotated the PA such that the principal axis of the Wollaston prism beam splitter was aligned perpendicular to the scattering plane, i.e., PA $\sim \Phi - 90^\circ$. In this configuration, symmetry dictates $P'_Q = P_Q$ and $P'_U = P_U = 0$, allowing us to save telescope time by taking exposures with δ angles corresponding to $X = Q$ only. Since we could not predict the exact timing (and hence, Φ) of the observations, we could not

set this alignment perfectly when submitting the VLT observing blocks (OBs). We corrected for these small deviations a posteriori by deriving $P_Q = P'_Q \sec(2\chi)$ (assuming $P_U = 0$), though in practice the correction was negligible (see Table 3). In the case of FoReRo2, which also has a Wollaston mask ($55'' \times 435''$), the PA of the instrument was not altered for the observations.

Appendix B
Data Reduction

During early epochs, 3I was projected against a crowded Galactic field, requiring careful rejection of frames contaminated by background stars overlapping the comet photocenter and their corresponding pair. After bias subtraction and flat field correction, for each valid exposure, we measured the $f^{\parallel}$and $f^{\perp}$ fluxes within circular apertures corresponding to a projected radius of ∼2000 km centered on the comet photocenter, subtracting the background sky contribution, which we measured in a nearby coma/tail-free sky region using sigma clipping to mitigate the effect of field stars. We opted for this small aperture size to reduce contamination from background stars. We then applied Equations (A1) and (A2) to measure numerical values of linear polarization. We use this method of aperture polarimetry to compare the bulk properties of 3I to that of other objects. To study the spatial distribution of polarization within the coma, we construct polarimetric maps from FORS2 data by aligning the whole $f^{\parallel}$and $f^{\perp}$ strips according to their photocenters and applying these same equations, and deep imaging maps by simply co-adding the aligned strips. We apply a Gaussian filter to the polarimetric maps to reduce noise in the image while preserving the overall structure and edges.

Finally, we observed zero- and high-polarization standard stars, VICyg12 and BD+28 4211, with ALFOSC to measure and correct for instrumental polarization, and BD+32 3739 and Hiltner 960 for FoReRo2. This was not necessary for FORS2, as standard star observations are already part of the instrument calibration plan. We calculated the uncertainties of the expressions following standard error propagation methods discussed, for instance, in S. Bagnulo et al. (2009).

ORCID iDs

Zuri Gray https://orcid.org/0000-0002-6610-1897
Stefano Bagnulo https://orcid.org/0000-0002-7156-8029
Galin Borisov https://orcid.org/0000-0002-4516-459X
Yuna G. Kwon https://orcid.org/0000-0002-8122-3606
Alberto Cellino https://orcid.org/0000-0002-6645-334X
Ludmilla Kolokolova https://orcid.org/0000-0002-9321-3202
Rosemary C. Dorsey https://orcid.org/0000-0002-8910-1021
Grigori Fedorets https://orcid.org/0000-0002-8418-4809
Mikael Granvik https://orcid.org/0000-0002-5624-1888
Eric MacLennan https://orcid.org/0000-0002-9870-123X
Olga Muñoz https://orcid.org/0000-0002-5138-3932
Philippe Bendjoya https://orcid.org/0000-0002-4278-1437
Maxime Devogèle https://orcid.org/0000-0002-6509-6360
Simone Ieva https://orcid.org/0000-0001-8694-9038
Antti Penttilä https://orcid.org/0000-0001-7403-1721
Karri Muinonen https://orcid.org/0000-0001-8058-2642

References

Alvarez-Candal, A., Barucci, M. A., Merlin, F., Guilbert, A., & de Bergh, C. 2007, A&A, 475, 369
Alvarez-Candal, A., Rizos, J. L., Lara, L. M., et al. 2025, A&A, 700, L10
Appenzeller, I. 1967, PASP, 79, 136
Bagnulo, S., Boehnhardt, H., Muinonen, K., et al. 2006, A&A, 450, 1239
Bagnulo, S., Cellino, A., Kolokolova, L., et al. 2021, NatCo, 12, 1797
Bagnulo, S., Landolfi, M., Landstreet, J. D., et al. 2009, PASP, 121, 993
Bagnulo, S., Tozzi, G. P., Boehnhardt, H., Vincent, J. B., & Muinonen, K. 2010, A&A, 514, A99
Barucci, M. A., Alvarez-Candal, A., Merlin, F., et al. 2011, Icar, 214, 297
Belskaya, I. N. 2013, Polarimetry of Transneptunian Objects and Centaurs V3.0, NASA Planetary Data System,
Belskaya, I. N., Bagnulo, S., Barucci, M. A., et al. 2010, Icar, 210, 472
Belskaya, I. N., Levasseur-Regourd, A. C., Shkuratov, Y. G., & Muinonen, K. 2008, in The Solar System beyond Neptune, ed. M. A. Barucci et al. (Tucson, AZ: Univ. Arizona Press), 115
Belyakov, M., Fremling, C., Graham, M. J., et al. 2025, RNAAS, 9, 194
Boehnhardt, H., Tozzi, G. P., Bagnulo, S., et al. 2008, A&A, 489, 1337
Bolin, B. T., Belyakov, M., Fremling, C., et al. 2025, MNRAS, 542, L139
Borisov, G., Bagnulo, S., Nikolov, P., & Bonev, T. 2015, P&SS, 118, 187
Bowell, E., West, R. M., Heyer, H. H., et al. 1992, IAUC, 5585, 1
Bus, S. J., & Binzel, R. P. 2002, Icar, 158, 146
Cellino, A., Bagnulo, S., Belskaya, I. N., & Christou, A. A. 2018, MNRAS, 481, L49
Cellino, A., Bagnulo, S., Gil-Hutton, R., et al. 2015, MNRAS, 451, 3473
Cellino, A., Bendjoya, P., Delbo', M., et al. 2020, A&A, 642, A80
Chandler, C. O., Bernardinelli, P. H., Jurić, M., et al. 2025, arXiv:2507.13409
Cordiner, M. A., Roth, N. X., Kelley, M. S. P., et al. 2025, ApJL, 991, L43
de la Fuente Marcos, R., Alarcon, M. R., Licandro, J., et al. 2025, A&A, 700, L9
Dehnen, W., Hands, T. O., & Schönrich, R. 2022, MNRAS, 512, 4078
Devogèle, M., Cellino, A., Borisov, G., et al. 2018, MNRAS, 479, 3498
Dougherty, L. M., & Geake, J. E. 1994, MNRAS, 271, 343
Flekkøy, E. G., & Toussaint, R. 2023, MNRAS, 523, L9
Frattin, E., Martikainen, J., Muñoz, O., et al. 2022, MNRAS, 517, 5463
Fulchignoni, M., Belskaya, I., Barucci, M. A., de Sanctis, M. C., & Doressoundiram, A. 2008, in The Solar System beyond Neptune, ed. M. A. Barucci et al. (Tucson, AZ: Univ. Arizona Press), 181
Gil-Hutton, R., Cellino, A., & Bendjoya, P. 2014, A&A, 569, A122
Gradie, J., & Tedesco, E. 1982, Sci, 216, 1405
Gray, Z., Bagnulo, S., Boehnhardt, H., et al. 2024a, MNRAS, 531, 1638
Gray, Z., Bagnulo, S., Granvik, M., et al. 2024b, PSJ, 5, 18
Guzik, P., Drahus, M., Rusek, K., et al. 2020, NatAs, 4, 53
Hadamcik, E., & Levasseur-Regourd, A. C. 2003, A&A, 403, 757
Hands, T. O., & Dehnen, W. 2020, MNRAS, 493, L59
Hasegawa, S., DeMeo, F. E., Marsset, M., et al. 2022, ApJL, 939, L9
Hasegawa, S., Marsset, M., DeMeo, F. E., et al. 2021, ApJL, 916, L6
Hergenrother, C. W., Adam, C. D., Chesley, S. R., & Lauretta, D. S. 2020, JGRE, 125, e06549
Hopkins, M. J., Dorsey, R. C., Forbes, J. C., et al. 2025, ApJL, 990, L30
Humes, O. A., Thomas, C. A., & McGraw, L. E. 2024, PSJ, 5, 80
Ishimaru, K., & Lauretta, D. S. 2024, MAPS, 59, 193
Ivanova, O., Rosenbush, V., Luk'yanyk, I., et al. 2023, A&A, 672, A76
Jewitt, D. 2004, AJ, 128, 3061
Jewitt, D., Hui, M.-T., Mutchler, M., Kim, Y., & Agarwal, J. 2025, ApJL, 990, L2
Kareta, T., Champagne, C., McClure, L., et al. 2025, ApJL, 990, L65
Kiselev, N., Rosenbush, V., Levasseur-Regourd, A.-C., & Kolokolova, L. 2015, Comets, 379 (Cambridge: Cambridge Univ. Press)
Kiselev, N., Shubina, E., Velichko, S., et al. 2017, Compilation of Comet Polarimetry from Published and Unpublished Sources, NASA Planetary Data System, 2017
Kwon, Y. G., Bagnulo, S., Markkanen, J., et al. 2024, AJ, 168, 164
Levasseur-Regourd, A.-C., Renard, J.-B., Shkuratov, Y., & Hadamcik, E. 2015, in Polarimetry of Stars and Planetary Systems, ed. L. Kolokolova, J. Hough, & A.-C. Levasseur-Regourd (Cambridge: Cambridge Univ. Press), 35
Lupishko, D. 2019, Asteroid Polarimetric Database (APD) V1.0, NASA Planetary Data System, doi:10.26033/z7xq-1x46
Mahlke, M., Carry, B., & Mattei, P. A. 2022, A&A, 665, A26
Meech, K. J., Weryk, R., Micheli, M., et al. 2017, Natur, 552, 378
Micheli, M., Farnocchia, D., Meech, K. J., et al. 2018, Natur, 559, 223
Muñoz, O., Moreno, F., Gómez-Martín, J. C., et al. 2020, ApJS, 247, 19
Muinonen, K., Penttilä, A., Cellino, A., et al. 2009, MAPS, 44, 1937
Opitom, C., Jehin, E., Hutsemékers, D., et al. 2021, A&A, 650, L19
Opitom, C., Snodgrass, C., Jehin, E., et al. 2025, MNRAS, 544, L31
Poch, O., Cerubini, R., Pommerol, A., Jost, B., & Thomas, N. 2018, JGRE, 123, 2564

Puzia, T. H., Rahatgaonkar, R., Carvajal, J. P., Nayak, P. K., & Luco, B. 2025, ApJL, 990, L27
Santana-Ros, T., Ivanova, O., Mykhailova, S., et al. 2025, arXiv:2508.00808
Seligman, D. Z., Micheli, M., Farnocchia, D., et al. 2025, ApJL, 989, L36
Shcherbina, M. P., Kiselev, N. N., Karpov, N. V., & Zhuzhulina, E. A. 2025, SoSyR, 59, 61
Shurcliff, W. A. 1962, JRASC, 56, 269
Taylor, A. G., & Seligman, D. Z. 2025, ApJL, 990, L14
Xing, Z., Oset, S., Noonan, J., & Bodewits, D. 2025, ApJL, 991, L50
Yang, B., Meech, K. J., Connelley, M., & Keane, J. V. 2025, arXiv:2507.14916
Zellner, B., & Gradie, J. 1976, AJ, 81, 262
Zubko, E., Videen, G., Shkuratov, Y., Muinonen, K., & Yamamoto, T. 2011, Icar, 212, 403